

Provided for non-commercial research and education use.
Not for reproduction, distribution or commercial use.



This article appeared in a journal published by Elsevier. The attached copy is furnished to the author for internal non-commercial research and education use, including for instruction at the authors institution and sharing with colleagues.

Other uses, including reproduction and distribution, or selling or licensing copies, or posting to personal, institutional or third party websites are prohibited.

In most cases authors are permitted to post their version of the article (e.g. in Word or Tex form) to their personal website or institutional repository. Authors requiring further information regarding Elsevier's archiving and manuscript policies are encouraged to visit:

<http://www.elsevier.com/copyright>



Contents lists available at ScienceDirect

International Journal of Heat and Mass Transfer

journal homepage: www.elsevier.com/locate/ijhmt

Transient response of PEM fuel cells with parallel and interdigitated flow field designs

Xiao-Dong Wang^{a,*}, Jin-Liang Xu^a, Wei-Mon Yan^b, Duu-Jong Lee^c, Ay Su^d

^a Beijing Key Laboratory of New and Renewable Energy, North China Electric Power University, Beijing 102206, China

^b Department of Greenergy, National University of Tainan, Tainan 700, Taiwan

^c Department of Chemical Engineering, College of Engineering, National Taiwan University of Science and Technology, Taipei 106, Taiwan

^d Department of Mechanical Engineering, Fuel Cell Center, Yuan Ze University, Taoyuan 300, Taiwan

ARTICLE INFO

Article history:

Received 13 February 2010

Received in revised form 16 December 2010

Accepted 20 December 2010

Available online 25 February 2011

Keywords:

Proton exchange membrane fuel cell

Transient characteristics

Two-phase flow

Response time

Overshoot and undershoot

ABSTRACT

Transient characteristics of proton exchange membrane (PEM) fuel cells with parallel and interdigitated flow fields upon changes in voltage load were investigated by applying a three-dimensional, two-phase model. Effects of channel to rib width ratios and cathode inlet flow rates on the transient response of PEM fuel cell were examined in detail. Current overshoot and undershoot occur because the time scale for the voltage change is much shorter than for the oxygen concentration changes. Therefore, the oxygen concentrations on the cathode diffusion layer-catalyst layer interface immediately after the voltage changes are essentially the same as before the voltage changes, which results in higher reaction rates causing overshoots when the voltage decreases or lower reaction rates causing undershoots when the voltage increases. The predictions also show that as the voltage decrease rate is reduced, the overshoot peak weakens and the response time shortens. Since the interdigitated flow field has higher oxygen concentrations on the cathode diffusion layer-catalyst layer interface due to the forced convection, the overshoot peaks and the undershoot valleys are all greater than for the parallel flow field. For both flow fields, larger channel to rib width ratios cause larger overshoots, smaller undershoots and longer response times.

© 2011 Elsevier Ltd. All rights reserved.

1. Introduction

Over the past decade, numerous efforts in terms of numerical modeling have been made to investigate the operation of proton exchange membrane fuel cell (PEMFC) [1–21]. Transient models for PEMFC predict their performances at start-up and shut-down processes for automotive applications.

Amphlett et al. [22] modeled the behavior of the stack temperature and the voltage during start-up, shut-down and load steps, with only the solid energy balance being modeled dynamically with all the other equations assumed to be quasi-steady for a given solid temperature. Lee and Lalk [23] investigated dynamic behavior of PEMFC stack using quasi-stationary models. Um et al. [24] developed a two-dimensional (2-D) fuel cell model with one figure showing the transient behavior describing the current overshoot corresponding to a step voltage change. The overshoot in local current density may severely deteriorate integrity of PEMFC.

Natarajan and Nguyen [25] presented a 2-D, two-phase, transient model for an isothermal PEMFC cathode. They concluded that liquid water transport would prolong the cell response time, especially under the current-collecting region. Wagner [26] showed

that the impedance of a fuel cell is a powerful tool to characterize the intra-electrode processes occurring in gas diffusion electrodes. Ceraolo et al. [27] developed a simplified, one-dimensional, transient model of a PEMFC based on SIMULINK to simulate the transient behavior of the cell voltage to a load change on a time-scale of seconds. Yerramalla et al. [28] conducted linear and non-linear analyses of a PEMFC system to describe whole, complex dynamic characteristics using SIMULINK. Golbert and Lewin [29] developed a transient along-the-channel 1-D model for a parallel flow field PEMFC incorporating mass balances of the liquid water and water vapor in evaporation, condensation and reaction. Friede et al. [30] developed a one-dimensional mathematical model to characterize the transient behavior of a PEMFC and concluded that the membrane water transport has a very strong influence on fuel cell transients. Shan and Choe [31] predicted the transient response of a PEMFC to an electric load change using a 2-D model that separated the fuel cell into several components, the membrane, catalysts, gas diffusion layer and bipolar plates. Pathapati et al. [32] solved for the transient response of the characteristic parameters of 2-D fuel cell to a step change in the current density using SIMULINK. Berg et al. [33] presented a half-cell transient discharge 3-D model for a delicately segmented PEMFC. Yan et al. [34–36] demonstrated a half-cell transient 2-D model capable of predicting the gas transport dynamics with respect to different channel/landing ratios and

* Corresponding author. Tel.: +86 10 6232 1277; fax: +86 10 8176 5088.

E-mail address: wangxd99@gmail.com (X.-D. Wang).

Nomenclature

$A_{0,a}^{\text{ref}}$	exchange current density at anode [A m^{-3}]
$A_{0,c}^{\text{ref}}$	exchange current density at cathode [A m^{-3}]
a	water activity
b	source term of variable ϕ
C	mass fraction
C_F	quadratic drag factor
D	mass diffusivity [$\text{m}^2 \text{s}^{-1}$]
$D_{k,\text{eff}}$	effective mass diffusivity for the k th species [$\text{m}^2 \text{s}^{-1}$]
d_{porous}	equivalent surface diameter of porous media [m]
F	Faraday constant [96,487 C/mol]
i	current density [A m^{-2}]
I	average current density in the fuel cell [A m^{-2}]
j_a	transfer current density at anode [A m^{-3}]
j_c	transfer current density at cathode [A m^{-3}]
k_c	coefficient of water vapor condensation rate [s^{-1}]
k_e	coefficient of water vapor evaporation rate [$\text{atm}^{-1} \text{s}^{-1}$]
k_p	permeability [m^2]
L_c	channel width [m]
L_r	rib width [m]
M	molecular weight [kg mol^{-1}]
p	pressure [atm]
p_{sat}	saturated water vapor pressure [atm]
P	perturbed variation of pressure in a control volume
R	Universal Gas Constant [$8.314 \text{ J mol}^{-1} \text{ K}^{-1}$]
s	volume ratio occupied by liquid water
S'	surface area [m^2]
S_c	source term in the species equation
S_j	source term in the phase potential equation
S_L	source term accounting for the phase change of water
$S_{\bar{u}}$	source term in the momentum equation
T	temperature [K]
t	time [s]
\bar{u}	velocity vector [m s^{-1}]
V	volume [m^3]
V_{cell}	operating voltage [V]
x	x direction coordinate [m]
y	y direction coordinate [m]
z	z direction coordinate [m]

Greek symbols

α_a	electrical transfer coefficient in forward reaction
α_c	electrical transfer coefficient in backward reaction
ε	porosity
ε_{eff}	effective porosity
η	over-potential [V]
λ	water content in membrane
ρ	density [kg m^{-3}]
σ_m	proton conductivity [S m^{-1}]
σ_s	electron conductivity [S m^{-1}]
τ	tortuosity of the pores in the porous material
Φ_m	ionic phase potential
Φ_m	electronic phase potential
ϕ	dependent variables
Ξ_ϕ	exchange coefficient

Superscripts

ref	reference value
-----	-----------------

Subscripts

a	anode
c	cathode
channel	channel
CL	catalyst layer
eff	effective
g	gaseous phase
k	k th species of the mixture
l	liquid phase
porous	porous medium
GDL	gas diffusion layer
H_2	hydrogen
H_2O	water
MEM	membrane
O_2	oxygen
sat	saturation
total	total

electrode porosities. Wang and Wang [37] developed a three-dimensional (3-D), single-phase, isothermal model to study the evolution of water accumulation and the corresponding transient response of the cell performance, where the effect of the mass transport of the gaseous reactants was not explicitly dictated. Their results demonstrated that the effect of water transport in the membrane is characterized by a timescale in the range of 10 s, whereas the charging and discharging of the electrochemical layer is very fast. Kumar and Reddy [38] studied the steady-state and transient performance of a 3-D PEMFC for different gas-flow channel shapes. Their results showed that it took about 10 s for the fuel cell to reach a new steady-state after a load change. Wang and Wang [39] studied based on a 2-D model the transient phenomena for current density step changes on a PEMFC, with a focus on dry cell operation. They concluded that a step increase in the current density instantaneously dries out the anode due to the influence of electro-osmotic drag. Song et al. [40] developed a transient one-dimensional non-isothermal two-phase PEMFC model to investigate transient liquid water transport in the cathode gas diffusion layer. Shimpalee et al. [41,42] numerically simulated the transient responses of a PEMFC subjected to variable load changes based on a 3-D, single-phase, isothermal PEMFC model. The simulations were conducted for a PEMFC with a serpentine flow-field and a 10 cm^2 reactive area. They presented numerical results for excess, normal, and minimal

fuel and air supplies. Wang and Wang [43] developed a two-phase transient model and analyzed the dynamics of gas diffusion layer dewetting and its impact on PEMFC performance. Wu et al. [44] developed a transient 2-D single-phase non-isothermal model of a PEMFC with the heat transfer equation to analyze the electro-chemical double-layer charging/discharging, species transport, membrane hydration/dehydration, and heat transfer processes. Based on their numerical results, these authors concluded that the heat transfer exerted a significant influence on the fuel cell dynamic response. Wu et al. [45] attempted to analyze the liquid water effect by defining a fixed liquid saturation of 10% in the porous materials in a PEMFC. Shah et al. [46] developed a transient non-isothermal model for a PEMFC. They presented numerical results using a 1-D model in the form of potential sweeps and were able to quantitatively predict the hysteresis phenomenon often observed in PEMFC experiments. However, their model was one-dimensional and, thus, could not be applied to fully investigate the complex multi-dimensional physics in practical PEMFC operations. Meng [47] developed a two-phase, non-isothermal, mixed-domain 2-D model to investigate 2-D PEMFC transient response and concluded that the liquid water in the porous materials increases the current density overshoots and undershoots.

Although researchers have developed various transient models to investigate the response characteristics of PEMFC, most of these

models have been one or two dimensional. Two-dimensional models are deficient in illustrating performance response of commercial PEMFC with complicated flow channels. Recently, some 3-D models have been developed but with single-phase and/or isothermal assumptions. Moreover, most studies have only focused on a step voltage change for a specified PEMFC flow field, with few analyses of the effect of the flow field type and flow field design parameters on the transient response characteristics. The present paper presents a 3-D, two-phase, transient PEMFC model to compare the transient characteristics of parallel and interdigitated flow fields. The effects of various voltage load changes, channel to rib width ratios, and cathode inlet flow rates on the current overshoot and undershoot and the cell response time are examined in detail for both flow fields.

2. Flow field design

The transient characteristics of PEMFC were investigated for parallel and interdigitated flow fields. Considering the symmetry, only the essential part of the fuel cell is analyzed as the computational domain to reduce the computational time. Fig. 1 shows the computational domains for both flow field designs which consist of the anode flow channel, anode diffusion layer, anode catalyst, proton exchange membrane, cathode catalyst layer, cathode diffusion layer, and cathode flow channel. For the parallel flow field, the computational domain includes a half flow channel and a half rib, while for the interdigitated flow field it includes a half inlet flow channel, a rib, and a half outlet flow channel. The effect of the

channel to rib width ratio on the transient characteristics were analyzed for three different width ratios for both flow fields. For cell 1, the flow channel width is 0.67 mm with a rib width of 1.33 mm. For cell 2, the flow channel and rib widths are both 1 mm. For cell 3, the flow channel width is 1.33 mm with a rib width of 0.67 mm. Thus, the channel to rib width ratios, λ , are 0.5, 1.0, and 2.0. The dimensions of all the cell components are listed in Table 1. Thicknesses for gas diffusion layer, catalyst layer and membrane were referred to experimental works by Yan et al. [48].

The operating conditions for the fuel cell were assumed to be a fuel cell temperature of 323 K, the reactant gases on the anode side include hydrogen and water vapor with a relative humidity of 100%, the reactant gases on the cathode side contain oxygen, nitrogen, and water vapor with a relative humidity of 100%, and the outlet pressures on the anode and cathode sides are both at 1 atm. Table 2 lists the inlet flow velocities for the parallel and interdigitated flow fields for the various channel to rib width ratios.

3. Model development

A 3-D two-phase, transient PEMFC model was developed to analyze the electrochemical reactions and transport phenomena of the reactants and products in the cell using the finite volume method. The governing equations included the mass, momentum, species and electrical potential conservation equations. The model assumes that the system is at transient state; the inlet reactants are ideal gases; the flow is laminar; and the porous layers such

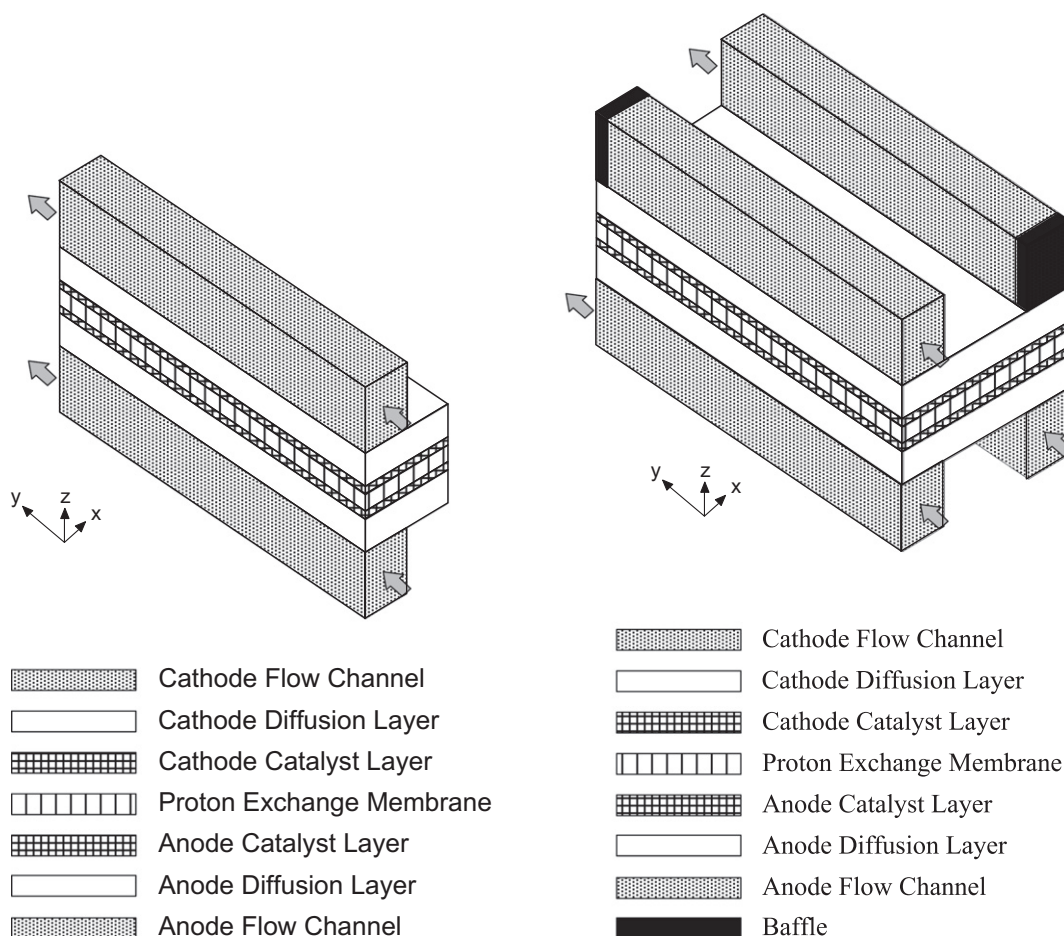


Fig. 1. Schematics of 3-D models of the parallel and interdigitated flow fields.

Table 1
PEM fuel cell dimensions.

Quantity	Value
Channel length (mm)	100
Channel height (mm)	1
Channel width (mm)	0.667, 1, 1.333
Rib length (mm)	100
Rib height (mm)	1
Rib width (mm)	1.333, 1, 0.667
Gas diffusion layer thickness (mm)	0.3
Catalyst layer thickness (mm)	0.005
Membrane thickness (mm)	0.035

Table 2
Cathode inlet velocities for the parallel and interdigitated flow fields for the various channel to rib width ratios.

λ	$V_{c,in}$ (m s ⁻¹)	
	Parallel flow field	Interdigitated flow field
2	0.7254	1.4508
1	0.9720	1.9440
0.5	1.4727	2.9454

as the diffusion layer, catalyst layer and PEM are isotropic and isothermal.

The transport equations for the gaseous phase in the 3-D PEMFC are:

Continuum equation:

$$\frac{\partial(\varepsilon_{\text{eff}}\rho_g)}{\partial t} + \nabla \cdot (\varepsilon\rho_g\vec{u}_g) = -S_L \quad (1)$$

where ε and ε_{eff} are the porosity and effective porosity of the porous material, ρ_g is the density of the gaseous mixture, and \vec{u}_g is the velocity vector for the gaseous mixture.

Momentum equation:

$$\begin{aligned} \frac{\varepsilon}{(1-s)} \frac{\partial(\rho_g\vec{u}_g)}{\partial t} + \frac{\varepsilon}{(1-s)^2} \nabla \cdot (\rho_g\vec{u}_g\vec{u}_g) \\ = -\varepsilon\nabla p_g + \frac{\varepsilon}{(1-s)} \nabla \cdot (\mu_g\nabla\vec{u}_g) + S_{ii} \end{aligned} \quad (2)$$

where s is the liquid water saturation defined as the ratio of the liquid water volume to the pore volume, μ_g is the viscosity of the gaseous mixture and S_{ii} is the source terms based on the Darcy drag forces imposed by the pore walls on the fluid which usually cause significant pressure drops across the porous media, which can be expressed as:

$$S_{ii} = -\frac{\varepsilon^2\mu_g\vec{u}_g}{k_p k_{rg}} - \frac{\varepsilon^3 C_F \rho_g}{\sqrt{k_p}} |\vec{u}_g| \vec{u}_g \quad (3)$$

where k_{rg} is the relative permeability for the gaseous mixture expressed as $k_{rg} = (1-s)^3$ which accounts for the reduction in pore space available for the gaseous phase due to the existence of the liquid phase, C_F is the quadratic drag factor, and k_p is the permeability of the porous material whose dependence on porosity can be described by the Blake–Kozeny equation [49]:

$$k_p = \left(\frac{d_{\text{porous}}^2}{150} \right) \left[\frac{\varepsilon^3}{(1-\varepsilon)^2} \right] \quad (4)$$

where d_{porous} is the equivalent pore diameter of the porous material expressed as $d_{\text{porous}} = 6V'_{\text{porous}}/S'_{\text{porous}}$.

Species equation:

$$\frac{\partial(\varepsilon_{\text{eff}}\rho_g C_k)}{\partial t} + \nabla \cdot (\varepsilon\rho_g\vec{u}_g C_k) = \nabla \cdot (\rho_g D_{k,\text{eff}} \nabla C_k) + S_c - S_L \quad (5)$$

where C_k is the mass fraction of the k th species and $D_{k,\text{eff}}$ is the effective diffusion coefficient with the Bruggeman correction [50] employed to describe the influence of the porosity on the diffusion coefficient

$$D_{k,\text{eff}} = D_k \varepsilon_{\text{eff}}^\tau \quad (6)$$

where τ is the tortuosity of the pores in the porous material. In the present two-phase model, the water produced in the cathode catalyst layer is assumed to be in the vapor phase, so in the species equation, the source term, S_c , in the catalyst layers due to chemical reactions equals $-(j_a/2F)M_{\text{H}_2}$ for hydrogen, $-(j_c/4F)M_{\text{O}_2}$ for oxygen, and $(j_c/2F)M_{\text{H}_2\text{O}}$ for water vapor. In these expressions, j_a and j_c denote the transfer current densities on the anode and cathode, respectively, calculated by the Butler–Volmer equation:

$$j_a = A_j^{\text{ref}} \left(\frac{C_{\text{H}_2}}{C_{\text{H}_2}^{\text{ref}}} \right)^{\frac{1}{2}} \left[e^{(\alpha_a F/RT)\eta} - \frac{1}{e^{(\alpha_c F/RT)\eta}} \right] \quad (7)$$

$$j_c = A_j^{\text{ref}} \left(\frac{C_{\text{O}_2}}{C_{\text{O}_2}^{\text{ref}}} \right) \left[e^{(\alpha_a F/RT)\eta} - \frac{1}{e^{(\alpha_c F/RT)\eta}} \right] \quad (8)$$

where A_j^{ref} is the reference exchange current density, α_a and α_c are the anodic and cathodic transfer coefficients for the anode and cathode reactions, η is the overpotential, F is Faraday's constant, R is the ideal gas constant and T is the fuel cell temperature.

In the catalyst layer, the potential difference between the electrolyte and catalyst drives the transfer current that maintains the electrochemical reaction. The current may be split into the ionic current, \vec{i}_m , and the electronic current, \vec{i}_s . The continuity of current leads to:

$$\nabla \cdot \vec{i}_m + \nabla \cdot \vec{i}_s = 0 \quad (9)$$

These two currents interact through the electrochemical reactions. Application of Ohm's law to this equation yields the current conservation:

$$\nabla \cdot (\sigma_m \nabla \Phi_m) = S_j \quad (10)$$

$$\nabla \cdot (\sigma_s \nabla \Phi_s) = -S_j \quad (11)$$

where σ_m and σ_s are the proton conductivity and electron conductivity, Φ_m and Φ_s are the ionic phase potential and electronic phase potential, and S_j is the electrical source term, which is zero in the PEM without the electrochemical reaction and is $-j_a$ or $-j_c$ on the anode or cathode sides. Based on the theoretical analyses in [37,45], since the electrochemical double-layer charging/discharging process is very fast, the transient terms in Eqs. (9)–(11) can be safely neglected. The proton conductivity in the membrane is strongly dependent on the membrane water content, λ , and can be calculated using the formulas developed by Springer [1]:

$$\sigma_m = \sigma_m^{\text{ref}} \exp \left[1268 \left(\frac{1}{303} - \frac{1}{T} \right) \right] \quad (12)$$

where σ_m^{ref} is the membrane reference conductivity expressed as

$$\sigma_m^{\text{ref}} = 0.5139\lambda - 0.326 \quad (13)$$

In the flow channels, gas diffusion layers and catalyst layers, the governing equation for the transport and formation of liquid water can be expressed by the generalized Richards equation:

$$\begin{aligned} \frac{\partial(\varepsilon\rho_l s)}{\partial t} + \nabla \cdot \left(\frac{\rho_l k_p k_{rl}}{\mu_l} \frac{\partial p_c}{\partial s} \nabla s \right) - \nabla \cdot \left(\frac{\rho_l k_p k_{rl}}{\mu_l} \nabla p_g \right) \\ + \nabla \cdot \left(\frac{n_d M_{\text{H}_2\text{O}}}{F} \vec{i}_m \right) = S_L \end{aligned} \quad (14)$$

where ρ_l is the density of liquid water, μ_l is the viscosity of liquid water, $M_{\text{H}_2\text{O}}$ is the molecular weight of water, k_{rl} is the relative permeability of liquid water equal to s^3 , and n_d is the electro-osmotic

drag coefficient taken as $n_d = 2.5s$. The electro-osmotic drag is only active in the catalyst layers where the ionic phase current exists, not in the channels and gas diffusion layers where the ionic phase current density is zero. The capillary pressure, p_c , is defined as

$$p_c = p_g - p_l \quad (15)$$

The capillary pressure can be further expressed as [37]

$$p_c = \sigma \cos \theta_c \left(\frac{r}{k_p} \right)^{1/2} (1.417(1-s) - 2.120(1-s)^2 + 1.262(1-s)^3) \quad \theta < 90^\circ$$

$$p_c = \sigma \cos \theta_c \left(\frac{r}{k_p} \right)^{1/2} (1.417s - 2.120s^2 + 1.262s^3) \quad \theta > 90^\circ \quad (16)$$

where σ is the surface tension of water and θ_c is the contact angle of water on the porous material.

When the water vapor partial pressure is greater than the water vapor saturation pressure, the water vapor is assumed to condense and fill the pores in the porous media. The source term, S_L , in Eqs. (1), (5) and (14), is a simplified switch function between condensation and/or evaporation of the liquid water evaluated as [17]:

$$S_L = \begin{cases} M_{H_2O} k_c \frac{\epsilon(1-s)x_{H_2O}}{RT} (p_{H_2O} - p_{sat}) & \text{if } p_{H_2O} > p_{sat} \\ k_e \epsilon s \rho_l (p_{H_2O} - p_{sat}) & \text{if } p_{H_2O} < p_{sat} \end{cases} \quad (17)$$

where k_c and k_e are the vapor condensation and evaporation rate constants, x_{H_2O} is the mole fraction of water vapor, and p_{sat} is the water vapor saturation pressure calculated as [37]:

$$p_{sat} = 10^{-2.1794 + 0.02953T - 9.1837 \times 10^{-5}T^2 + 1.4454 \times 10^{-7}T^3} \quad (18)$$

Assuming water exists only in the liquid phase in the membrane, the liquid water transport equation in the membrane can be expressed as:

$$\frac{\partial(\rho_{dry} M_{H_2O} \lambda / M_m)}{\partial t} + \nabla \cdot \left(\left(\frac{\alpha_d M_{H_2O} \bar{z}}{F} i_m \right) \lambda - \left(\frac{M_{H_2O} \rho_{dry}}{M_m} D_\lambda \right) \nabla \lambda \right) = 0 \quad (19)$$

where α_d is a constant equal to 2.5/22, ρ_{dry} is the membrane dry density, M_m is the membrane equivalent weight, and D_λ is the diffusivity expressed as a function of the membrane water content as [1]:

$$D_\lambda = D_\lambda^{ref} \exp \left(2416 \left(\frac{1}{303} - \frac{1}{T} \right) \right) \quad (20)$$

$$D_\lambda^{ref} = 10^{-10} \frac{\lambda}{(1 + 0.0126\lambda)a(17.81 - 79.7a + 108a^2)D'_\lambda} \quad (21)$$

$$D'_\lambda = \begin{cases} \lambda/4 & \lambda \leq 2 \\ 0.5 + 3.25(\lambda - 2)/4 & \lambda \leq 6 \\ 3.75 + 4(\lambda - 26)/15 & \lambda > 6 \end{cases} \quad (22)$$

where a is the water activity.

At the interface between the membrane and catalyst layer, the water content is related to the water activity as [1]:

$$\lambda = \begin{cases} 0.043 + 17.18a - 39.85a^2 + 36.0a^3 & 0 < a \leq 1 \\ 14 + 1.4(a - 1) & 1 < a \leq 3 \\ 16.8 & a > 3 \end{cases} \quad (23)$$

where, a is the water activity expressed as:

$$a = \frac{C_{H_2O} RT}{p_{sat}} \quad (24)$$

The conservation equation of the water content, Eq. (19), is linked to water vapor concentration by two internal boundary conditions at the interfaces between the membrane and the two

catalyst layers on both anode and cathode sides. The interfacial boundary conditions can be established based on thermodynamic equilibrium conditions and flux equalities. The detail boundary conditions can be referred in Meng's work [51].

The overpotentials are defined as:

$$\eta = \Phi_s - \Phi_m \quad \text{on anode side} \quad (25)$$

$$\eta = \Phi_s - \Phi_m - V_{oc} \quad \text{on cathode side} \quad (26)$$

where V_{oc} is the open-circuit potential defined as [2]:

$$V_{oc} = 1.23 - 0.9 \times 10^{-3}(T - 298) + 2.3 \frac{RT}{4F} \left(\log p_{H_2}^2 p_{O_2} \right) \quad (27)$$

The fuel cell voltage is given by

$$V_{cell} = V_{oc} - \eta_a - \eta_c - \eta_m \quad (28)$$

where η_m is the Ohmic overpotential in the membrane defined as:

$$\eta_m = \int_{mem} \frac{i_{ave}}{\sigma_m} dz \quad (29)$$

The boundary conditions at the anode flow channels and the cathode flow channels are that the inlet flow rates are constant, the inlet gas compositions are constant, and the flows are fully developed at the anode and cathode flow channels outlets. The solid walls are no slip with zero flux boundary conditions. At the interfaces between the gas channels, the gas diffusion layers, the catalyst layers, and the PEM, the velocities, mass fractions, momentum fluxes, and mass fluxes are all assumed equal. The computational domain for the electrical charge equations included the anode catalyst layer, the membrane and the cathode catalyst layer. The boundary conditions included: at the interface of the anode catalyst layer: $\Phi_s = 0$, $\partial \Phi_m / \partial z = 0$; at the interface of the cathode catalyst layer: $\Phi_s = V_{cell}$, $\partial \Phi_m / \partial z = 0$. All of the fixed parameters used in the model can be found in [52]. There have been efforts to refine the material parameters describing water transport in GDL, MPL, and so on (see Ref. [52, and listed therein]). The parameters adopted in this work are to demonstrate the transient response and mechanisms responsible for the noted response of fuel cells with different flow fields. Use of refined parameters does not affect the basic trends numerically yielded using the present material parameters.

The coupled equations were solved iteratively using computational fluid dynamics package FLUENT (version 6.3, Ansys, USA). Iteration criterion for convergence was 10^{-6} . The model used non-uniformly distributed elements in the x , y and z directions. The grid independence was examined in preliminary test runs. Fig. 2 shows the predicted local current densities along the center line of the flow channel in the membrane for the parallel flow field

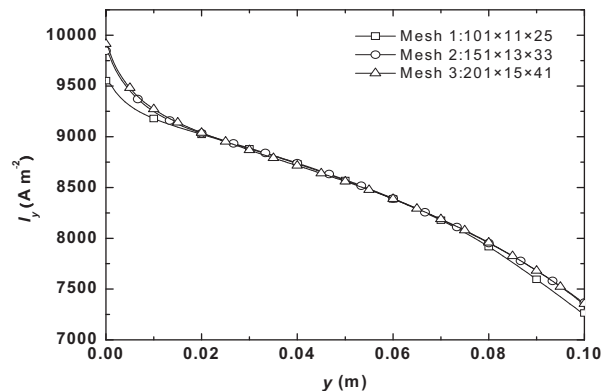


Fig. 2. Influence of the number of elements on the local current densities for the parallel flow field design with $\lambda = 1.0$.

with $\lambda = 1.0$. The results show that the $151 \times 13 \times 33$ mesh for the parallel flow field and the $151 \times 25 \times 33$ mesh for the interdigitated flow field can provide sufficient spatial resolution. The independence of the time step size, Δt , was also examined as shown in Fig. 3 with Δt then taken as 0.01 s except for the Case 2 in Fig. 4 which $\Delta t = 0.005$ s. The accuracy of the present transient model was demonstrated by Li et al. [53].

The temperature change in the PEM fuel cell is not taken into account in the present model, i.e. isothermal model is used. This is because we focus on a single cell with a small dimension. Although the electrochemical reaction and the phase change of water produce heat, the produced heat flux is low and the thermal conductivities of the porous layers and the bipolar plates are high. Wang et al. have demonstrated that with the constant temperature boundary condition applied at surfaces of anode/cathode current collectors, the isothermal and non-isothermal models predict almost the same performance and the operation temperature of a single fuel cell with a small dimension can be kept almost constant in all the regions of the working fuel cell [54].

4. Results and discussion

4.1. Voltage loading effects

Four different voltage reduction rates (from 0.7 V to 0.5 V) were selected to investigate the effect of the voltage loading on the transient characteristics of the parallel flow field fuel cell. Case 1 had a

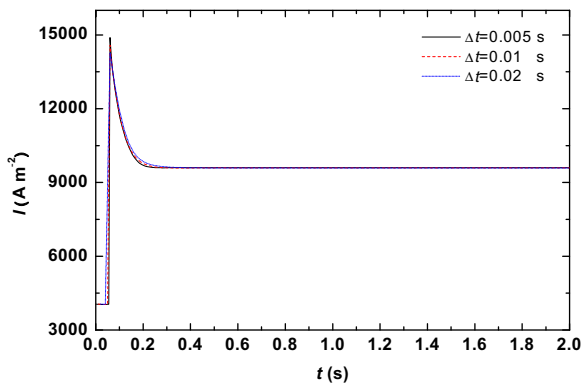


Fig. 3. Influence of the time step size on the transient response of the average current densities during a step voltage decrease for the parallel flow field for $\lambda = 1.0$.

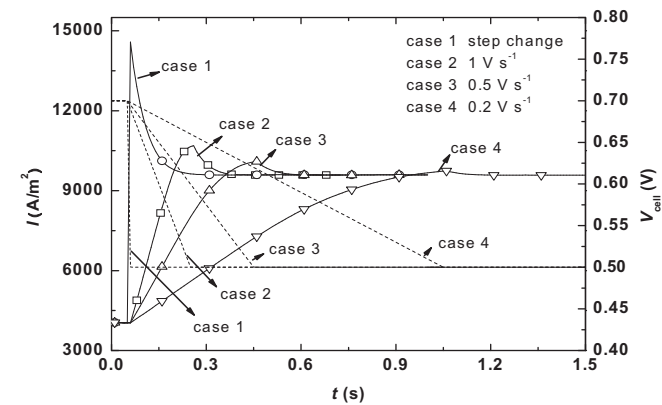


Fig. 4. Transient response of the parallel flow field fuel cell for $\lambda = 1.0$ for the various voltage reduction rates. Solid line: average current density; dashed line: voltage.

step voltage change with $V_{\text{cell}} = 0.7$ V for $t < 0.05$ s, $V_{\text{cell}} = 0.5$ V for $t > 0.05$ s; Cases 2–4 had voltage decrease rates of 1 V s^{-1} , 0.5 V s^{-1} , and 0.2 V s^{-1} starting at $t = 0.06$ s. Fig. 4 shows that for the step voltage change in the parallel flow field design for $\lambda = 1$, the average current density abruptly increases to $14,580 \text{ A m}^{-2}$ at 0.06 s with the strongest current overshoot, then begins to decrease at 0.29 s to steady-state at 0.5 V with a response time of 0.24 s. For Case 2, the average current density begins to increase at 0.06 s, exceeds the steady-state value at 0.5 V at 0.195 s, reaches the maximum of $10,688 \text{ A m}^{-2}$ at 0.26 s, and then gradually decreases to steady-state at 0.40 s with a response time of 0.14 s. For Case 3, the average current density begins to increase at 0.06 s, overshoot occurs at 0.36 s, the average current density reaches the maximum of $10,093 \text{ A m}^{-2}$ at 0.46 s, and then decreases to steady-state at 0.59 s with a response time of 0.13 s. For Case 4, the average current density begins to increase at 0.06 s, overshoot occurs at 0.96 s, the average current density reaches the maximum of 9744 A m^{-2} at 1.06 s, and then decreases to steady-state at 1.15 s with a response time of 0.09 s. These results indicate that as the voltage decrease rate is reduced, the overshoot weakens and the response time shortens.

To fully understand which factors affect the current overshoot and response time, the step voltage change results were analyzed to describe the local dynamic transport characteristics inside the cell. Fig. 5 shows the transient response of the local current densities along the center line of the channel and rib in the membrane. At $t = 0.01$ s, the cell is at the steady-state of 0.7 V. With the weak electrochemical reaction rates at the high operating voltage of 0.7 V, the local current density is distributed uniformly over the membrane. At 0.06 s, the voltage is abruptly reduced to 0.5 V, the local current density rapidly rises with a small difference developing between the values under the channel and under the rib, so the local current density is still relatively uniform over the membrane. The maximums of the local current density under the channel and rib both occur at the cell inlet with the local current density gradually decreasing from the inlet to the outlet. At 0.10 s, the local current densities under the channel and rib are both lower than at 0.06 s with a more significant decrease under the rib; thus, the difference in the local current densities under the channel and under the rib has increased. Moreover, the gradient in the local current densities from the inlet to the outlet also increases as the distribution becomes non-uniform over the membrane. At 0.24 s, the local current densities under the channel and the rib are further reduced and more non-uniform. At 0.29 s, the local current density distribution approaches steady-state with a response time of 0.24 s.

Fig. 6 shows the transient response of the oxygen concentrations along the center line of the channel and rib on the cathode

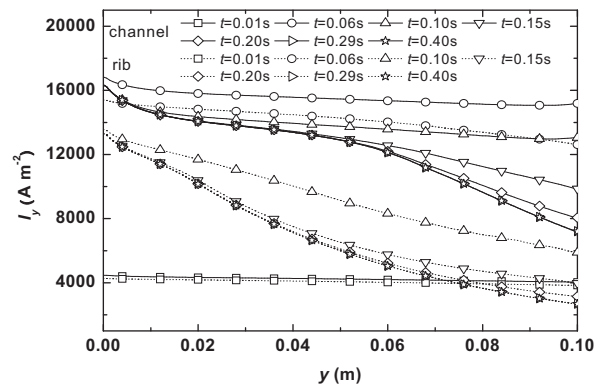


Fig. 5. Transient response of the local current densities along the center line of the channel and the rib in the membrane during a step voltage change for the parallel flow field design for $\lambda = 1.0$.

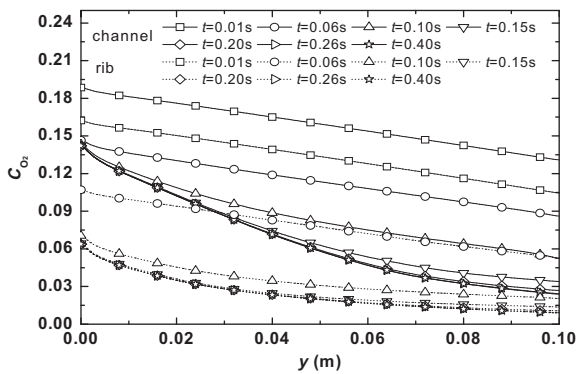


Fig. 6. Transient response of the oxygen concentrations along the center line of the channel and the rib at the cathode diffusion layer-catalyst layer interface during a step voltage change for the parallel flow field design for $\lambda = 1.0$.

diffusion layer-catalyst layer interface for the step voltage change for the parallel flow field design for $\lambda = 1.0$. Fig. 6 indicates that at $t = 0.01$ s, there are high, uniform oxygen concentrations under the channel and rib because the electrochemical reactions are weaker with a small amount of oxygen consumption at the high operating voltage of 0.7 V. At 0.06 s, the voltage is abruptly reduced to 0.5 V, which causes the electrochemical reactions to rapidly increase. Since the high oxygen concentrations under the channel and the rib at this time supply the electrochemical reactions, the local current densities under the channel and the rib simultaneously rapidly increase with small differences between them. Therefore, the current overshoot can be attributed to the initially high, uniform local oxygen concentrations inside the cell when the voltage abruptly decreases. The higher local oxygen concentration will increase the overshoot, as will be verified later. At 0.10 s, the local oxygen concentration decreases from that at 0.06 s as the oxygen consumption by the electrochemical reactions is higher than the transport from the flow channel, which leads to reduced local current densities. With a longer diffusion path, the oxygen concentration under the rib decreases more significantly than under the channel; thus, the decrease in the local current density under the rib is more visible as shown in Fig. 5. Subsequently, the oxygen concentrations under the channel and the rib continue to decrease until it reaches the steady-state values at 0.5 V. The oxygen concentrations approach steady-state at 0.20 s which is slightly faster than the response time for the current density of 0.26 s. Therefore, the initial oxygen concentrations are far higher than the steady-state concentrations at the low voltage which leads to the current overshoot and significantly affects the local

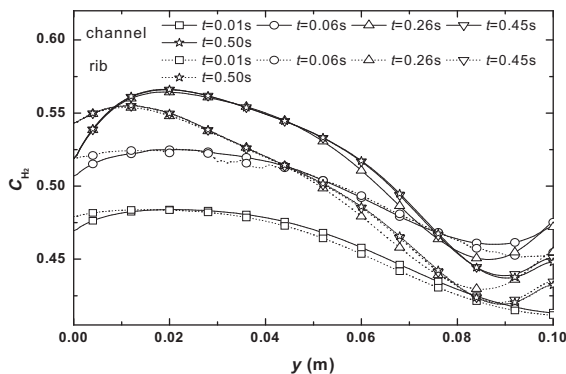


Fig. 7. Transient response of the hydrogen concentrations along the center line of the channel and the rib at the anode diffusion layer-catalyst layer during a step voltage change for the parallel flow field design for $\lambda = 1.0$.

current density distribution, but it is not a decisive factor for the cell response time.

Fig. 7 shows the transient response of the hydrogen concentrations along the center line of the channel and the rib on the anode diffusion layer-catalyst layer interface for the step voltage change for the parallel flow field design for $\lambda = 1.0$. Fig. 7 indicates that as the voltage decreases from 0.7 V to 0.5 V, the hydrogen concentration gradually increases. Although the hydrogen consumption increases along with the increasing electrochemical reaction, there is also a net water transport from the anode to the cathode along with the proton transport, which causes the relative hydrogen concentration to increase because the molecular weight of water is much larger than that of hydrogen. Fig. 7 also indicates that due to the lower anode inlet flow velocity, the hydrogen concentration still does not reach the steady-state value at 0.45 s, so the hydrogen concentration is also not a key factor determining the response time.

Fig. 8 shows the transient response of liquid water concentration along the channel center and the rib at the anode diffusion layer-catalyst layer upon a step voltage change for the parallel flow field design at $\lambda = 1.0$. Since water transport response time (in the scale of 100 s) is much greater than that for reactant (product) transfer (in the scale of 1 s) [55], the liquid water concentration at 0.54 s does not change much from that at $t = 0.01$ s (the steady-state of 0.7 V), although the current density has approached a steady-state of 0.5 V.

Fig. 9(a) shows the transient response of the local current densities at $y = 0.05$ m along the cell width direction in the membrane for the four different voltage reduction rates for the parallel flow field design with $\lambda = 1.0$. At $t = 0.01$ s, for the four cases, the cells are all at the steady-state voltage of 0.7 V, the local current densities under the channel and the rib are uniformly distributed due to the lower electrochemical reaction rates. For Case 1, the voltage abruptly decreases from 0.7 V to 0.5 V at 0.06 s causing the average current density to sharply increase to the maximum and a local current density gradient to develop from the channel ($15,462 \text{ A m}^{-2}$) to the rib ($14,275 \text{ A m}^{-2}$), so the local current densities are still distributed relatively uniformly. For Case 2, with a voltage reduction rate of 1 V s^{-1} starting at 0.06 s to 0.5 V at 0.26 s where the peak overshoot of the average current density occurs. Moreover, for Case 2 the local current densities under the channel and the rib are significantly lower than for Case 1, and the difference between the local current densities under the channel and under the rib increases (from $13,364 \text{ A m}^{-2}$ under the channel center to 7315 A m^{-2} under the rib center), so the non-uniformity of the local current density distribution is much more evident. With the slower voltage reduction rates, the overshoot

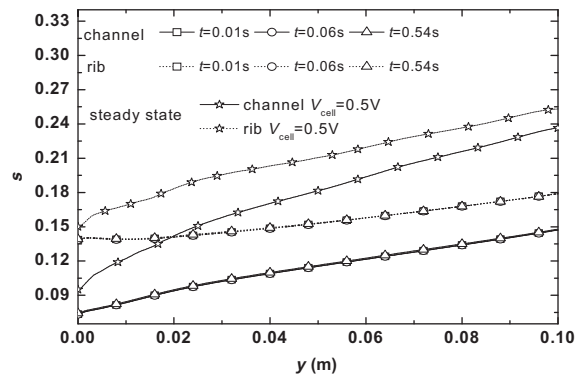


Fig. 8. Transient response of the liquid water concentrations along the center line of the channel and the rib at the anode diffusion layer-catalyst layer during a step voltage change for the parallel flow field design for $\lambda = 1.0$.

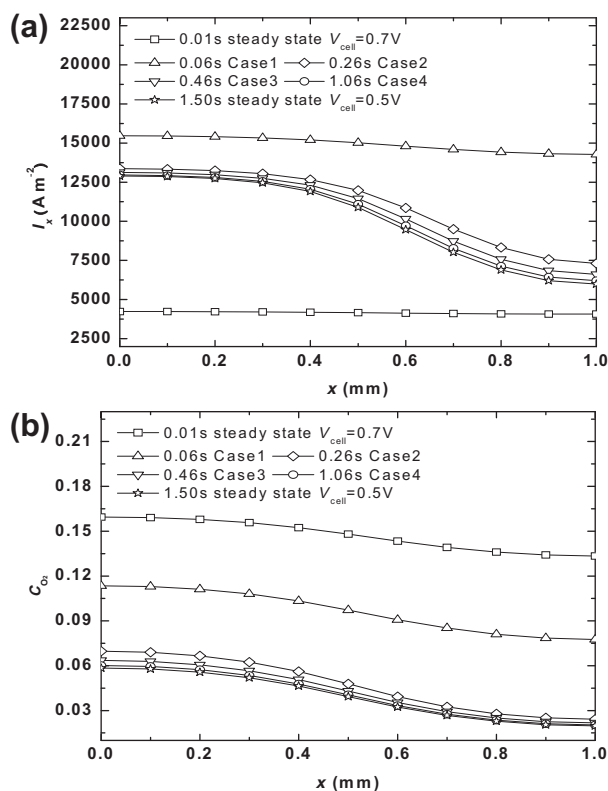


Fig. 9. Comparison of the transient responses for the four different voltage reduction rates for the parallel flow field design for $A = 1.0$. (a) Local current densities; (b) local oxygen concentrations.

peaks of the average current densities are further reduced for Case 3 and Case 4. The average current densities reach peaks at 0.46 s for Case 3 and at 1.06 s for Case 4, with the local current density distribution differences from the channel to the rib become more non-uniform and closer to the steady-state distribution at 0.5 V.

Fig. 9(b) shows the transient response of the oxygen concentrations at $y = 0.05$ m along the cell width direction on the cathode diffusion layer-catalyst layer interface for the four different voltage reduction rates. When the cell is at the steady-state voltage of 0.7 V at 0.01 s, there are high oxygen concentrations at the cathode diffusion layer-catalyst layer interface. For Case 1, as the voltage abruptly decreases to 0.5 V at 0.06 s, the oxygen concentrations are still high, which results in the strongest overshoot. From Case 2 to Case 4, voltage reduction rate gradually decreases, a longer time is available for the oxygen concentrations to decrease; thus, the current overshoot becomes less than for Case 1. As the time for the voltage to decrease from 0.7 V to 0.5 V becomes longer, the local oxygen concentrations become lower and closer to the steady-state distribution for 0.5 V with less overshoot and shorter response times. These results further verify that the higher local oxygen concentrations cause more overshoot.

Fig. 10 shows the transient response of the parallel flow field fuel cell for $A = 1.0$ during a sinusoidal voltage change between 0.8 V and 0.6 V ($V_{cell} = 0.7 - 0.1 \times \sin(t - 0.05)$). For comparison, Fig. 10(a) also shows the transient response of the average current density for a step voltage increase from 0.7 V to 0.8 V and a step voltage decrease from 0.7 V to 0.6 V. Fig. 10(a) indicates that along with the sinusoidal change in the voltage, the current density also changes sinusoidally with no current overshoot as the voltage decreases to 0.6 V and no undershoot as the voltage increases to 0.8 V. Fig. 10(b) compares the local current density distributions at $t = 1.63$ s ($V_{cell} = 0.6$ V) for the step and sinusoidal voltage

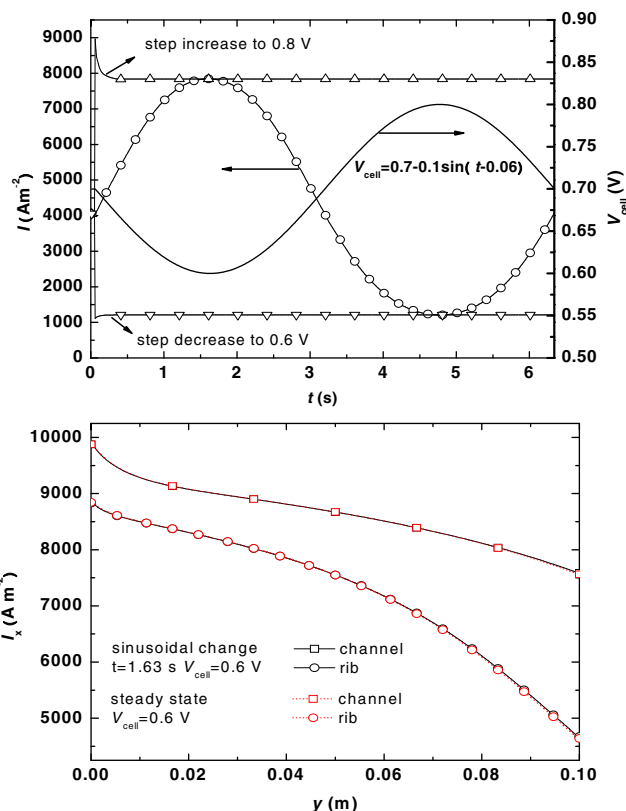


Fig. 10. Transient responses of the parallel flow field fuel cell for $A = 1.0$ during a sinusoidal voltage change. (a) Average current density; (b) local current density.

changes, which indicates that when the voltage decreases to 0.6 V along a sinusoidal path, the local current densities under the channel and under the rib are almost the same as for the steady-state voltage of 0.6 V. Therefore, the current overshoot and undershoot can be eliminated by controlling the voltage change.

4.2. Comparison of parallel and interdigitated flow fields

The flow field design in the bipolar plates has a very important effect on the steady-state performance of a PEMFC because different flow field designs provide the different reactant transport and liquid water removal rates. The previous analyses have shown that the overshoot, undershoot, and response time are all related to the oxygen concentration and the membrane water content; thus, it is expected that the flow field design will also affect the transient characteristics of a PEMFC. Thus, this section will analyze the different transient responses of the parallel and interdigitated flow fields.

Fig. 11 shows the transient response of the average current densities for both flow fields during a step voltage change. At $t \leq 0.05$ s, the both cells are all at the steady-state of 0.7 V and have almost the same performance with slightly better performance for the interdigitated flow field. At $t = 0.06$ s, the voltage abruptly decreases to 0.5 V, the average current density sharply increases to the maximum and the overshoot occurs with peaks of 15,299 A m⁻² for the interdigitated flow field and 14,580 A m⁻² for the parallel flow field, indicating that the interdigitated flow field has a more overshoot. Later, the average current density is gradually reduced to the steady-state value of 0.5 V. For the parallel flow field, the steady-state average current density is 9587 A m⁻² with a response time of 0.24 s, while it is

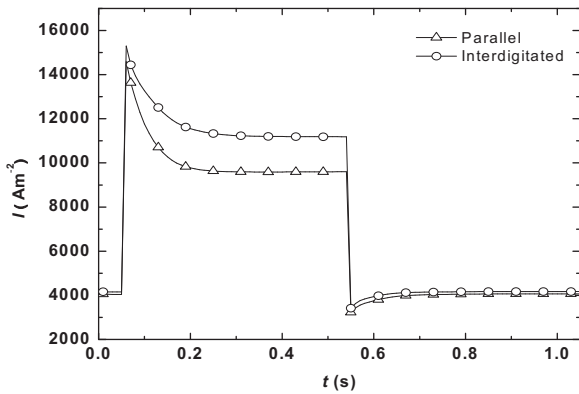


Fig. 11. Transient responses of the average current densities for the parallel and interdigitated flow fields during step voltage changes.

11,187 A m⁻² for the interdigitated flow field with a response time of 0.36 s.

Fig. 12(a) shows the transient response of the local current densities in the membrane at $y = 0.05$ m along the cell width direction for both flow fields. The interdigitated flow field flow channel can be divided into an inlet channel and an outlet channel. In Fig. 12, $x < 0.5$ mm corresponds to the inlet channel, $0.5 \text{ mm} < x < 1.5$ mm corresponds to the rib, and $1.5 \text{ mm} < x < 2.0$ mm corresponds to the outlet channel. For both flow fields, at $t = 0.01$ s, the local current density distributions are very uniform over the membrane. At 0.06 s, the local current densities sharply rise and then slowly decrease along the x -direction, indicating that the local current density distributions are still uniform over the membrane. At 0.15 s, for the parallel flow field the local current density already approaches the steady-state distribution with the local current

density under the channel far higher than that under the rib, showing a non-uniform local current density distribution. However, for the interdigitated flow field, the local current density is still quite different from the steady-state distribution (the difference occurs under the outlet channel) with a significantly non-uniform distribution. The local current density reaches steady-state at 0.29 s for the parallel flow field and at 0.41 s for the interdigitated flow field, indicating that the interdigitated flow field has a longer response time. During the transient response, the local current density for the interdigitated flow field is higher than that for the parallel flow field all the time, so it has a stronger overshoot.

Fig. 12(b) shows the transient response of the oxygen concentrations on the cathode diffusion layer-catalyst layer interface at $y = 0.05$ m along the cell width direction for the both flow fields. At $t = 0.01$ s, there are high local oxygen concentrations for both flow fields with the interdigitated flow field having a higher oxygen concentration than the parallel flow field. Since both cells are still at the steady-state of 0.7 V at this time with a very little difference between the average current densities, and the oxygen consumption rates by the electrochemical reactions are almost the same, thus, the interdigitated flow field can transport more oxygen to the gas diffusion layer and catalyst layer. At 0.06 s, the voltage abruptly decreases to 0.5 V; since there are still higher oxygen concentrations on the cathode diffusion layer-catalyst layer interface for both flow fields, the average current densities are higher than the steady-state value of 0.5 V; thus, the overshoot occurs. At this moment, due to the uniform local oxygen concentration distributions for both flow fields the local current densities are still distributed relatively uniformly. With the higher local oxygen concentration, the interdigitated flow field produces a higher local current density than the parallel flow field and more overshoot. At 0.15 s, the local oxygen concentration already approaches the steady-state distribution for the parallel flow field, while for the interdigitated flow field the oxygen concentration under the outlet channel is still slightly larger than at the steady-state distribution. Therefore, the interdigitated flow field needs longer time for the oxygen concentration to reach the steady-state distribution, resulting in a longer response time than for the parallel flow field.

Fig. 11 also shows the transient response of the average current densities for both flow fields during a step voltage increase. At $t = 0.54$ s, both flow fields are all at the steady-state of 0.5 V. At 0.55 s, the voltage abruptly increases to 0.7 V, so the average current densities are sharply reduced, lower than the steady-state value of 0.5 V for both flow fields, so current undershoot occurs with a more undershoot for the parallel flow field. The average current densities for both flow fields then gradually rise. The parallel flow field reaches steady-state at 0.78 s, while the interdigitated flow field reaches steady-state at 0.73 s, indicating that the parallel flow field has a longer response time during step voltage increase, which is opposite to what occurs during the step voltage decrease.

Fig. 13(a) shows the transient response of the local current densities in the membrane at $y = 0.05$ m along the cell width direction for the flow fields during the step voltage increase. At $t = 0.54$ s, the interdigitated flow field has a higher local current density than the parallel flow field and for both flow fields the local current densities are reduced along the cell width direction with significant variations. At 0.55 s, for both flow fields the local current densities sharply decrease as the voltage abruptly increases from 0.5 V to 0.7 V. The local current densities still vary along the cell width direction and are lower than the steady-state value of 0.7 V, which results in the current undershoot. The local current densities for both flow fields then gradually increase and become more uniform. For the parallel flow field, the local current density reaches steady-state at 0.78 s, while for the interdigitated flow field it reaches steady-state at 0.73 s.

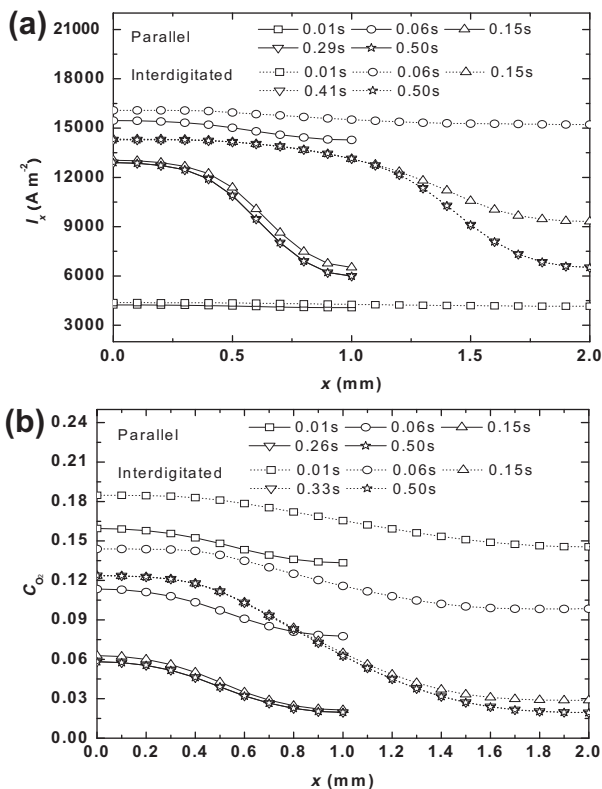


Fig. 12. Transient responses of the parallel and interdigitated flow fields during step voltage decreases. (a) Local current densities; (b) oxygen concentrations.

Fig. 13(b) shows the transient response of the local oxygen concentrations on the cathode diffusion layer-catalyst layer at $y = 0.05$ m along the cell width direction for both flow fields during a step voltage increase. At $t = 0.54$ s, both cells are at the steady-state of 0.5 V and the local oxygen concentrations are very low and non-uniformly distributed along the cell width direction. At 0.55 s when the voltage abruptly increases to 0.7 V, the lower local oxygen concentrations result in lower local current densities than the steady-state densities at 0.7 V, which results in undershoot. Moreover, the local current density distributions are not uniform for both flow fields due to the non-uniform oxygen concentration distributions. At 0.55 s the parallel flow field has a lower oxygen concentration than the interdigitated flow field, so the parallel flow field deviates more from the steady-state of 0.7 V, with more undershoot. At 0.60 s, the oxygen concentration for the interdigitated flow field approaches steady-state under the inlet channel, while still deviating from steady-state under the rib and outlet channel. However, for the parallel flow field, at 0.60 s, the local oxygen concentrations under the channel and rib all significantly deviate from the steady-state value. At 0.78 s, although the oxygen concentration has not completely reached steady-state, the local current density no longer increases because the oxygen provided for the cathode catalyst layer already satisfies the need of the electrochemical reactions. For the interdigitated flow field, there is similar phenomenon at 0.73 s where the oxygen concentration has not reached steady-state, but the local current density no longer increases. These results again indicate that the cell response time is not determined by the oxygen concentration distribution.

4.3. Size effects

The channel to rib width ratio, λ , significantly affects the steady-state performance of a PEMFC. Wang et al. [18] found that for the parallel flow field, as λ increases the cell performance improves because the reactants are transported into the diffusion layer and the catalyst layer mainly by diffusion. A larger λ increases the contact area between the reactants and the diffusion layer, which allows more reactants to diffuse directly into the porous layers to participate in the electrochemical reaction which enhances the reaction rates. For the interdigitated flow field, the baffle forces more reactants to enter the cell and participate in the electrochemical reaction, so λ has less effect. λ is also expected to affect the transient characteristics of the PEMFC; therefore, this section will discuss the effect of λ on the transient response of the parallel and interdigitated flow fields.

Fig. 14(a) shows the transient response of the parallel flow field with various channel to rib width ratios during a step voltage change. For the parallel flow field, the optimal steady-state performance occurs for $\lambda = 2.0$ with the worst steady-state performance for $\lambda = 0.5$. During the step voltage decrease, the voltage abruptly decreases from 0.7 V to 0.5 V at $t = 0.06$ s. For the cell with $\lambda = 2.0$, the average current density reaches a maximum of $14,943 \text{ A m}^{-2}$ at 0.06 s and reaches steady-state at 0.33 s with the strongest overshoot and a response time of 0.28 s. For the cell with $\lambda = 1.0$, the average current density reaches a maximum of $14,580 \text{ A m}^{-2}$ at 0.06 s and reaches steady-state at 0.29 s with the less overshoot and a response time of 0.24 s. For the cell with $\lambda = 0.5$, the average current density reaches a maximum of $13,640 \text{ A m}^{-2}$ at 0.06 s and reaches steady-state at 0.24 s with the weakest overshoot and a response time of 0.19 s. During the step voltage increase, the voltage abruptly increases from 0.5 V to 0.7 V at $t = 0.55$ s. For the cell with $\lambda = 2.0$, the average current density reaches steady-state at 0.86 s with the weakest undershoot and a response time of 0.31 s. For the cell with $\lambda = 1.0$, the average current density reaches steady-state at 0.83 s with more undershoot and a response time of 0.28 s. For the cell with $\lambda = 0.5$, the average current density

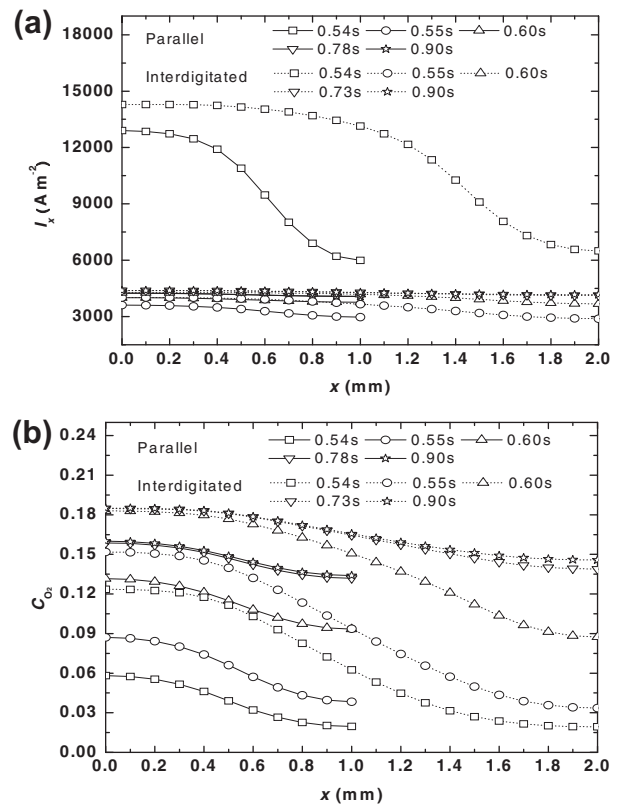


Fig. 13. Transient responses of the parallel and interdigitated flow fields during step voltage increases. (a) Local current densities; (b) oxygen concentrations.

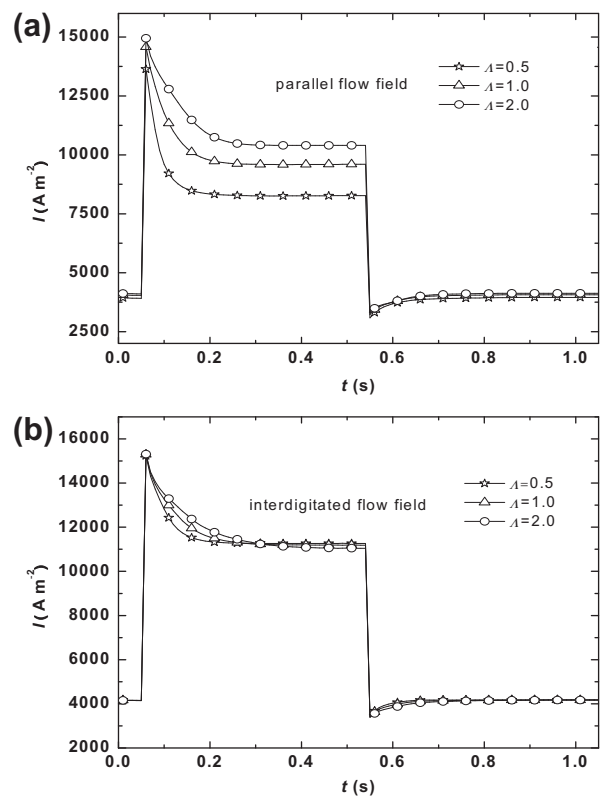


Fig. 14. Transient responses of the parallel and interdigitated flow fields for various channel to rib width ratios during step voltage changes. (a) Parallel flow field; (b) interdigitated flow field.

reaches steady-state at 0.80 s with the strongest undershoot and a response time of 0.25 s. These results indicate that for the parallel flow field, cells with larger Λ have more overshoot, less undershoot, and longer response times. The longer response times can be attributed to the lower cathode inlet velocities for the cell with larger Λ .

Fig. 14(b) shows the transient response for the interdigitated flow field with various channel to rib width ratios during a step voltage change. For the interdigitated flow field, Λ has little effect on the steady-state performance. For the cell with $\Lambda = 0.5$, which has the best steady-state performance, the average current density reaches a maximum of $15,236 \text{ A m}^{-2}$ at $t = 0.06 \text{ s}$ and a minimum of 3451 A m^{-2} at 0.56 s . For the cell with $\Lambda = 1.0$ the average current density reaches a maximum of $15,299 \text{ A m}^{-2}$ at $t = 0.06 \text{ s}$ and a minimum of 3419 A m^{-2} at 0.56 s , while for the cell with $\Lambda = 2.0$, which has the worst steady-state performance, the average current density reaches a maximum of $15,312 \text{ A m}^{-2}$ at $t = 0.06 \text{ s}$ and a minimum of 3381 A m^{-2} at 0.56 s . Therefore, for the interdigitated flow field, cells with larger Λ have more overshoot and less undershoot along with the worst steady-state performance. As with the parallel flow field, as Λ increases the response time increases for the interdigitated flow field. Therefore, for the interdigitated flow field, a smaller Λ not only slightly improves the steady-state performance but also reduces the cell transient response time.

4.4. Cathode inlet flow velocity effects

Fig. 15 shows the transient response of the parallel and interdigitated flow fields for various cathode inlet velocities during step voltage changes. Fig. 15 shows that for both flow fields a higher cathode inlet velocity only slightly increases the steady-state

performance at 0.7 V, but significantly improves the steady-state performance at 0.5 V. During the step voltage changes, the higher cathode inlet velocities results in the more overshoot, less undershoot, and shorter cell response times.

5. Conclusion

A 3-D, two-phase, transient model was adopted to investigate the transient characteristics of PEMFC with the parallel and interdigitated flow fields. The effects of various voltage load changes, channel to rib width ratios, and cathode inlet velocities on the response time, the current overshoot and undershoot were analyzed in detail. The conclusions drawn from the analyses are:

1. The voltage reduction rate significantly affects the transient characteristics of PEMFC. The overshoot peak was reduced and the response time declined at low voltage decreasing rate. The step voltage decrease created the strongest overshoot and the longest response time. The sinusoidal voltage change does not create the overshoot and undershoot.
2. The overshoot and undershoot are related to the local oxygen concentration distributions. During the voltage decrease, the high, uniform oxygen concentration at the initially high voltage induces the overshoot. On the contrary, during the voltage increase, the initially low, non-uniform oxygen concentration at the initially low voltage induces undershoot.
3. Since the interdigitated flow field yields higher local oxygen concentration than does the parallel flow field owing forced convection effect, the former has more significant overshoot and less profound undershoot.
4. The channel to rib width ratio also significantly affects the transient characteristics of the parallel flow field but has less influence on the interdigitated flow field. For both flow fields, a larger channel to rib width ratio causes more overshoot, less undershoot and longer response times.

Acknowledgement

This study was supported by the National Natural Science Foundation of China (No. 50876009) and the National Natural Science Foundation of China for Distinguished Young Scholars (No. 50825603).

References

- [1] T.E. Springer, T.A. Zawodinski, S. Gottesfeld, Polymer electrolyte fuel-cell model, *J. Electrochem. Soc.* 138 (1991) 2334–2342.
- [2] D.M. Bernardi, M.W. Verbrugge, Mathematical-model of a gas-diffusion electrode bonded to a polymer electrolyte, *AIChE J.* 37 (1991) 1151–1163.
- [3] T.F. Fuller, J. Newman, Water and thermal management in solid-polymer-electrolyte fuel-cells, *J. Electrochem. Soc.* 140 (1993) 1218–1225.
- [4] T.V. Nguyen, R.E. White, A water and heat management model for proton exchange membrane fuel cells, *J. Electrochem. Soc.* 140 (1993) 2178–2186.
- [5] V. Gurau, F. Barbir, H. Liu, An analytical solution of a half-cell model for PEM fuel cells, *J. Electrochem. Soc.* 47 (2000) 2468–2477.
- [6] J.S. Yi, T.V. Nguyen, An along-the-channel model for proton exchange membrane fuel cells, *J. Electrochem. Soc.* 145 (1998) 1149–1159.
- [7] J.S. Yi, T.V. Nguyen, Multicomponent transport in porous electrodes of proton exchange membrane fuel cells using the interdigitated gas distributors, *J. Electrochem. Soc.* 146 (1999) 38–45.
- [8] W.B. Gu, C.Y. Wang, B.Y. Liaw, Numerical modeling of coupled electrochemical and transport processes in lead-acid batteries, *J. Electrochem. Soc.* 144 (1997) 2053–2061.
- [9] S. Um, C.Y. Wang, K.S. Chen, Computational fluid dynamics modeling of proton exchange membrane fuel cells, *J. Electrochem. Soc.* 147 (2000) 4485–4493.
- [10] N. Djilali, D. Lu, Influence of heat transfer on gas and water transport, *Int J. Thermal Sci.* 41 (2002) 29–40.
- [11] S.H. Ge, B.L. Yi, A mathematical model for PEMFC in different flow modes, *J. Power Sources* 124 (2003) 1–11.
- [12] N.P. Siegel, M.W. Ellis, D.J. Nelson, M.R. von Spakovsky, Single domain PEMFC model based on agglomerate catalyst geometry, *J. Power Sources* 115 (2003) 81–89.

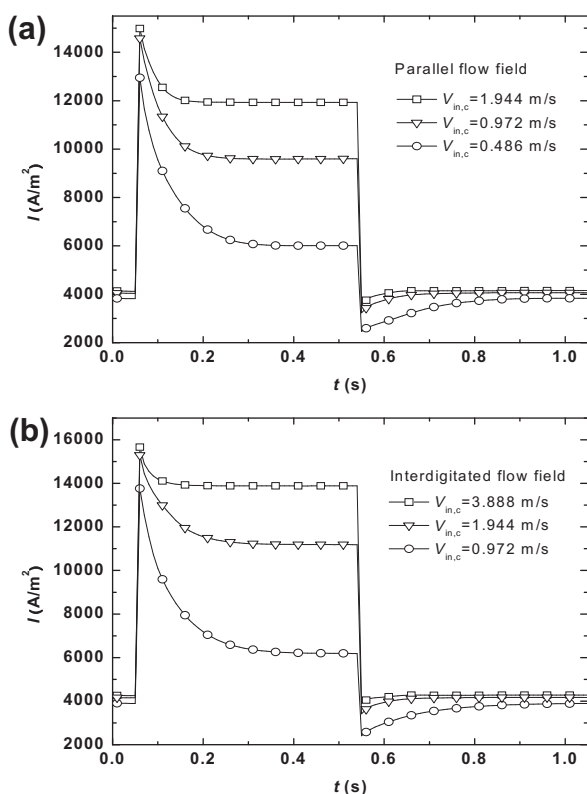


Fig. 15. Transient responses of the parallel and interdigitated flow fields for various cathode inlet flow velocities during step voltage changes. (a) Parallel flow field; (b) interdigitated flow field.

- [13] S. Mazumder, J.V. Cole, Rigorous 3-D mathematical modeling of PEM fuel cells I. Model predictions without liquid water transfer, *J. Electrochem. Soc.* 150 (2003) A1503–A1509.
- [14] S. Mazumder, J.V. Cole, Rigorous 3-D mathematical modeling of PEM fuel cells II. Model predictions with liquid water transfer, *J. Electrochem. Soc.* 150 (2003) A1510–A1517.
- [15] C.Y. Wang, Fundamental models for fuel cell engineering, *Chem. Rev.* 104 (2004) 4727–4766.
- [16] S. Shimpalee, S. Greenway, D. Spuckler, J.W. Van Zee, Predicting water and current distributions in a commercial-size PEMFC, *J. Power Sources* 135 (2004) 79–87.
- [17] S. Shimpalee, S. Greenway, J.W. Van Zee, The impact of channel path length on PEMFC flow-field design, *J. Power Sources* 160 (2006) 398–406.
- [18] X.D. Wang, Y.Y. Duan, W.M. Yan, Numerical study of cell performance and local transport phenomena in PEM fuel cells with various flow channel area ratios, *J. Power Sources* 172 (2007) 265–277.
- [19] X.D. Wang, Y.Y. Duan, W.M. Yan, X.F. Peng, Effects of flow channel geometry on cell performance for PEM fuel cells with parallel and interdigitated flow fields, *Electrochim. Acta* 53 (2008) 5334–5343.
- [20] X.D. Wang, Y.Y. Duan, W.M. Yan, F.B. Weng, Effect of humidity of reactants on the cell performance of PEM fuel cells with parallel and interdigitated flow field designs, *J. Power Sources* 176 (2008) 247–258.
- [21] X.D. Wang, Y.Y. Duan, W.M. Yan, X.F. Peng, Local transport phenomena and cell performance of PEM fuel cells with various serpentine flow field designs, *J. Power Sources* 175 (2008) 397–407.
- [22] J. Amphlett, R. Mann, B. Peppley, P. Roberge, A. Rodrigues, A model predicting transient responses of proton exchange membrane fuel cells, *J. Power Sources* 61 (1996) 183–188.
- [23] J. Lee, T. Lalk, Modeling fuel cell stack systems, *J. Power Sources* 73 (1998) 229–241.
- [24] S. Um, C.Y. Wang, K.S. Chen, Computational fluid dynamics modeling of proton exchange membrane fuel cells, *J. Electrochem. Soc.* 147 (2000) 4485–4493.
- [25] D. Natarajan, T.V. Nguyen, A two-dimensional, two-phase, multicomponent, transient model for the cathode of a proton exchange membrane fuel cell using conventional gas distributors, *J. Electrochem. Soc.* 148 (2001) A1324–A1335.
- [26] N. Wagner, Characterization of membrane electrode assemblies in polymer electrolyte fuel cells using a.c. impedance spectroscopy, *J. Appl. Electrochem.* 32 (2002) 859–863.
- [27] M. Ceraolo, C. Miulli, A. Pozio, Modelling static and dynamic behaviour of proton exchange membrane fuel cells on the basis of electro-chemical description, *J. Power Sources* 113 (2003) 131–144.
- [28] S. Yerramalla, A. Davari, A. Faliachi, Modeling and simulation of the dynamic behavior of a polymer electrolyte membrane fuel cell, *J. Power Sources* 124 (2003) 104–113.
- [29] J. Golbert, D. Lewin, Model-based control of fuel cells: regulatory control, *J. Power Sources* 135 (2004) 135–151.
- [30] W. Friede, S. Rael, B. Davat, Mathematical model and characterization of the transient behavior of a PEM fuel cell, *IEEE Trans. Power Electron.* 19 (2004) 1234–1241.
- [31] Y. Shan, S. Choe, A high dynamic PEM fuel cell model with temperature effects, *J. Power Sources* 145 (2005) 30–39.
- [32] P.R. Pathapati, X. Xue, J. Tang, A new dynamic model for predicting transient phenomena in a PEM fuel cell system, *Renewable Energy* 30 (2005) 1–22.
- [33] P. Berg, K. Promislow, J. Stumper, B. Wetton, Discharge of a segmented polymer electrolyte membrane fuel cell, *J. Fuel Cell Sci. Technol.* 2 (2005) 111–120.
- [34] W.M. Yan, C.Y. Soong, F. Chen, H.S. Chu, Transient analysis of reactant gas transport and performance of PEM fuel cells, *J. Power Sources* 143 (2005) 48–56.
- [35] J. Zhou, X.F. Peng, W.M. Yan, Dynamic analysis of gas transport in cathode side of PEM fuel cell with interdigitated flow field, *J. Power Sources* 159 (2006) 514–523.
- [36] W.M. Yan, H.S. Chu, J.Y. Chen, C.Y. Soong, F. Chen, Transient analysis of water transport in PEM fuel cells, *J. Power Sources* 162 (2006) 1147–1156.
- [37] Y. Wang, C.Y. Wang, Transient analysis of polymer electrolyte fuel cells, *Electrochim. Acta* 50 (2005) 307–1315.
- [38] A. Kumar, R.G. Reddy, Effect of gas flow-field design in the bipolar/end plates on the steady and transient state performance of polymer electrolyte membrane fuel cells, *J. Power Sources* 155 (2006) 264–271.
- [39] Y. Wang, C.Y. Wang, Dynamics of polymer electrolyte fuel cells undergoing load changes, *Electrochim. Acta* 51 (2006) 3924–3933.
- [40] D. Song, Q. Wang, Z.S. Liu, C. Huang, Transient analysis for the cathode gas diffusion layer of PEM fuel cells, *J. Power Sources* 159 (2006) 928–942.
- [41] S. Shimpalee, W.K. Lee, J.W. Van Zee, H. Naseri-Neshat, Predicting the transient response of a serpentine flow-field PEMFC I. Excess to normal fuel and air, *J. Power Sources* 156 (2006) 355–368.
- [42] S. Shimpalee, W.K. Lee, J.W. Van Zee, H. Naseri-Neshat, Predicting the transient response of a serpentine flow-field PEMFC II: normal to minimal fuel and air, *J. Power Sources* 156 (2006) 369–374.
- [43] Y. Wang, C.Y. Wang, Two-phase transients of polymer electrolyte fuel cells, *J. Electrochem. Soc.* 154 (2007) B636–B643.
- [44] H. Wu, P. Berg, X. Li, Non-isothermal transient modeling of water transport in PEM fuel cells, *J. Power Sources* 165 (2007) 232–243.
- [45] H. Wu, X. Li, P. Berg, Numerical analysis of dynamic processes in fully humidified PEM fuel cells, *Int. J. Hydrogen Energy* 32 (2007) 2022–2031.
- [46] A.A. Shah, G.S. Kim, P.C. Sui, D. Harvey, Transient non-isothermal model of a polymer electrolyte fuel cell, *J. Power Sources* 163 (2007) 793–806.
- [47] H. Meng, Numerical investigation of transient responses of a PEM fuel cell using a two-phase non-isothermal mixed-domain model, *J. Power Sources* 171 (2007) 738–746.
- [48] W.M. Yan, C.H. Yang, C.Y. Soong, F. Chen, S.C. Mei, Experimental studies on optimal operating conditions for different flow field designs of PEM fuel cells, *J. Power Sources* 160 (2006) 284–292.
- [49] F.A.L. Dullien, *Porous Media*, Academic Press, New York, 1991.
- [50] W. He, J.S. Yi, T.V. Nguyen, Two-phase flow model of the cathode of PEM fuel cells using interdigitated flow fields, *AIChE J.* 46 (2000) 2053–2064.
- [51] H. Meng, A two-phase non-isothermal mixed-domain PEM fuel cell model and its application to two-dimensional simulations, *J. Power Sources* 168 (2007) 218–228.
- [52] X.D. Wang, X.X. Zhang, W.M. Yan, D.J. Lee, A. Su, Determination of the optimal active area for proton exchange membrane fuel cells with parallel, interdigitated or serpentine designs, *Int. J. Hydrogen Energy* 34 (2009) 3823–3832.
- [53] H.Y. Li, W.C. Weng, W.M. Yan, X.D. Wang, Transient characteristics of proton exchange membrane fuel cells with different flow field designs, *J. Power Sources* 196 (2010) 235–245.
- [54] X.D. Wang, X.X. Zhang, W.M. Yan, D.J. Lee, A. Su, Non-isothermal effects of single or double serpentine proton exchange membrane fuel cells, *Electrochim. Acta* 55 (2010) 4926–4934.
- [55] K. Fushinobu, K. Shimizu, N. Miki, K. Okazaki, Optical measurement technique of water contents in polymer membrane for PEFCs, *J. Fuel Cell Sci. Technol.* 3 (1) (2006) 13–17.